ID29: a high-intensity highly automated ESRF beamline for macromolecular crystallography experiments exploiting anomalous scattering

**Daniele de Sanctis,[a] Antonia Beteva,[a] Hugo Caserotto,[a] Fabien Dobias,[a]
José Gabadinho,[a]‡ Thierry Giraud,[a] Alexandre Gobbo,[b] Matias Guijarro,[a]
Mario Lentini,[a] Bernard Lavault,[b] Trevor Mairs,[a] Seán McSweeney,[a]
Sébastien Petitdemange,[a] Vicente Rey-Bakaikoa,[a] John Surr,[a]
Pascal Theveneau,[a] Gordon A. Leonard[a]* and Christoph Mueller-Dieckmann[a]***

[a]European Synchrotron Radiation Facility, 6 rue Jules Horowitz, 38043 Grenoble, France, and [b]EMBL-Grenoble Outstation, 6 rue Jules Horowitz, 38042 Grenoble, France. E-mail: leonard@esrf.fr, muellerd@esrf.fr

ID29 is an ESRF undulator beamline with a routinely accessible energy range of between 20.0 keV and 6.0 keV (λ = 0.62 Å to 2.07 Å) dedicated to the use of anomalous dispersion techniques in macromolecular crystallography. Since the beamline was first commissioned in 2001, ID29 has, in order to provide an improved service to both its academic and proprietary users, been the subject of almost continuous upgrade and refurbishment. It is now also the home to the ESRF Cryobench facility, ID29S. Here, the current status of the beamline is described and plans for its future are briefly outlined.

Keywords: macromolecular crystallography; anomalous scattering; ESRF; automation; long wavelengths.

1. Introduction

The first macromolecular crystallography (MX) beamline dedicated to the MAD (multiwavelength anomalous dispersion) technique to be constructed at the European Synchrotron Radiation Facility (ESRF) was BM14, commissioned in early 1996 (Biou *et al.*, 1997). Unusually for an ESRF public access facility, the beamline was allocated a bending magnet as a source of X-rays. An undulator-based MAD beamline, ID14-4 (Wakatsuki *et al.*, 1998; McCarthy *et al.*, 2009), was commissioned at the ESRF in 1998.

While both BM14 and ID14-4 are highly successful facilities, each has its drawbacks. The large focal spot size of BM14 (0.4 mm × 0.8 mm; V × H, FWHM) means that the collection of diffraction data from small crystals is problematic, and a lack of X-ray flux at either end of its accessible energy range makes experiments at $E > 17$ keV (*i.e.* U L_{III} absorption edge; $\lambda \simeq 0.73$ Å) and $E < 7$ keV (*i.e.* Fe K absorption edge; $\lambda \simeq 1.77$ Å) extremely time-consuming. The increased brilliance of the X-ray beam on ID14-4 facilitates the measurement of diffraction data from small crystals. However, the 'Quadriga' approach used in the construction of the ID14 complex (Wakatsuki *et al.*, 1998) means that ID14-4 is not an independent beamline and changing undulator gaps in order to target different absorption edges affects the intensity of the X-ray beam of the other three end-stations on ID14. Moreover, absorption by the beam splitters used to provide X-rays to the three ID14 side-stations means that, for ID14-4, photon flux at softer X-ray energies ($E \leq 9$ keV; $\lambda \geq 1.38$ Å) is severely attenuated. This makes MAD/SAD experiments at longer wavelengths impractical or impossible on ID14-4.

Taking into account these disadvantages, the burgeoning use of anomalous scattering techniques in MX and the clear need to expand its beamline portfolio in the area, the ESRF took the decision to construct a second undulator-based MAD beamline on the straight section ID29. The perceived advantages of the new facility were that it would complement ID14-4, providing a fully independent beamline with a relatively small beam size and suitable photon flux over the entire wavelength range (6–20 keV; λ = 0.62 Å to 2.07 Å) routinely used for MX phasing experiments exploiting anomalous scattering.

Routine user operation of ID29 began in 2001. Since then, diffraction data collected on the beamline have contributed to more than 1000 depositions to the Protein Data Bank (wwPDB; Berman *et al.*, 2000). The beamline is also extensively used for proprietary research. We describe here the current status of the beamline and briefly outline plans for its future.

2. Beamline layout, X-ray source and optical configuration

The overall layout of ID29 is shown in Fig. 1(*a*), and its optical configuration and beam characteristics are summarized in Table 1. The beamline is divided into two autonomously functioning sections: primary slits, monochromator, secondary slits and focusing mirror are located in the optics hutch (OH); sample-defining slits, sample environment, fast shutter, diffractometer and detector are located in the experimental hutch (EH).

2.1. X-ray source

The ID29 low-β straight section is equipped with two undulators as sources of X-rays (Fig. 2*a*): a 1.6 m ESRF U$_{35}$ device with a minimum

doi:10.1107/S0909049512009715

beamlines

Table 1
The optical configuration and beam characteristics of ID29.

|	
X-ray source	1.6 m U_{35} in-air (minimum gap 16 mm), 2.0 m in-vacuum U_{21} undulator (minimum gap 6 mm) mounted in series
Source size (r.m.s., H × V)	59 µm × 8.3 µm
Source divergence (r.m.s., H × V)	90 µrad × 3 µrad
Monochromator (energy range)	Channel-cut Si[111] (5.2–20 keV); channel-cut Si[311] (9.6–20 keV)
Focusing element	Toroidal mirror with Rh coating: useful area 700 mm × 40 mm; incident angle 3 mrad; sagittal radius 39.5 mm ± 0.1 mm
Demagnification ratio	3:1
Energy range	6.0–20.0 keV
Higher harmonic rejection	Double flat Si mirror system, grazing angle 3 mrad; rejection ratio $\sim 10^{-4}$
Flux at sample position	4.5×10^{12} photons s^{-1} (at 11.56 keV; 200 mA stored current)
Spot size at sample position (H × V; FWHM)	60 µm × 30 µm

gap of 16 mm and a 2 m ESRF U_{21} device with a minimum gap of 6 mm. The latter operates *in vacuo*. Although the two undulators are installed in series, to limit the heat load on the channel-cut monochromator (see below) only one of these sources is operated at any one time (*i.e.* U_{21} for 8.5 keV < E < 15 keV; U_{35} for E < 8.5 keV and E > 15 keV). Downstream of the X-ray source the photon beam passes through an ESRF standard high-power front-end which is separated from the beamline optics hutch by a 300 µm-thick chemical-vapour-deposition diamond window (Biasci *et al.*, 2002).

2.2. Optical configuration

Following experience gained during the operation of ID14-4, a minimalist optical configuration was adopted for ID29 [Fig. 1(a), Table 1]. In particular, a liquid-nitrogen-cooled Si [111] channel-cut monochromator (CCM) was chosen for energy selection. While CCMs are non-fixed-exit devices, they are much easier to operate and maintain than their double-crystal counterparts, and vertical beam movements resulting from energy changes can be dealt with by a straightforwardly calculated displacement of elements downstream on the beamline. Indeed, the positive experience with the CCM installed on ID29 led to a similar device being used in the construction of ESRF beamline ID23-1 (Nurizzo *et al.*, 2006), and the replacement, during the recent refurbishment of ID14-4 (McCarthy *et al.*, 2009), of the originally installed double-crystal monochromator by a CCM.

The ID29 monochromator vessel contains two CCMs. The second CCM is a monolithic Si [311] crystal designed to provide increased energy resolution in MAD/SAD experiments. Switching between the Si [111] and Si [311] crystals is straightforward, with the latter
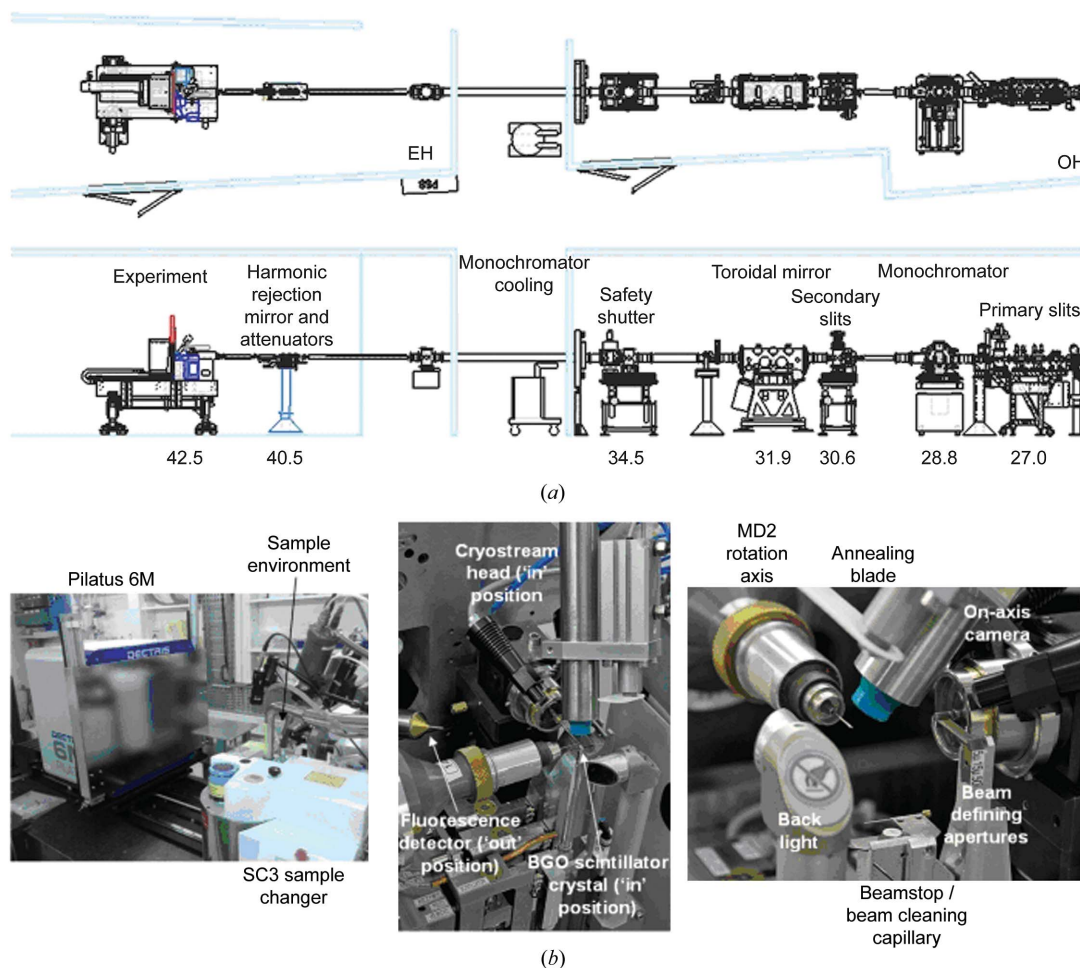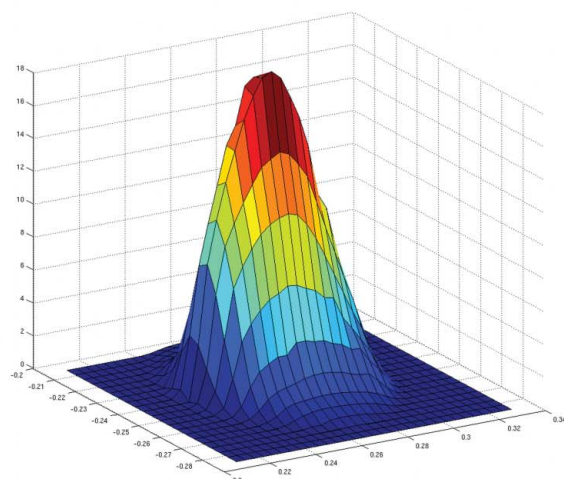

Figure 1
The overall layout of ID29. (*a*) Top and side views of the overall layout of ID29 with distances in metres from the source of each of the elements in the optics (OH) and experimental (EH) hutches shown. For clarity, diagnostic tools along the beamline are not labelled. (*b*) The experimental set-up on ID29 showing an overall view (left), and two close-up views of the sample environment. Major components are labelled.
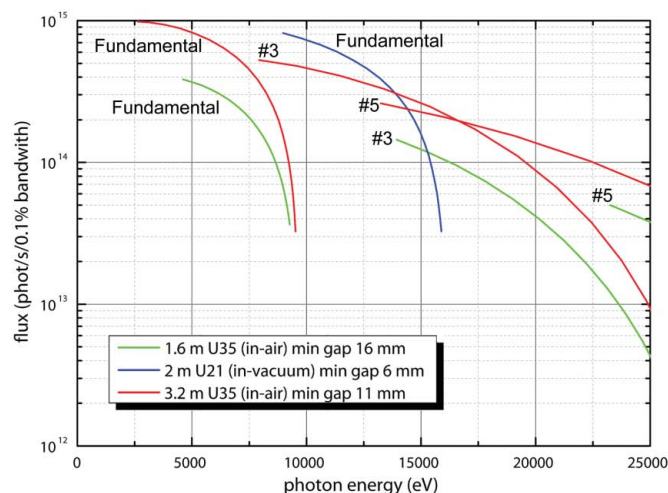
(a)

(b)
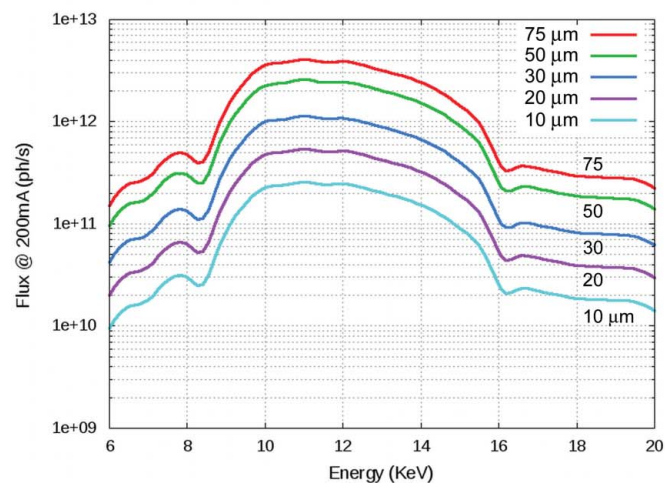
(c)

Figure 2
ID29 X-ray source, beam size and flux at the sample position. (*a*) The output spectra of the two undulators (U$_{35}$ green, U$_{21}$ blue) that currently serve as radiation sources [photons s^{-1} (0.1% bandwidth)$^{-1}$ through a 3 mm (H) × 1 mm (V) pinhole at 30 m]. Also shown (green) is the output spectrum of an in-air 3.2 m ESRF U$_{35}$ undulator with 11 mm minimum gap. (*b*) Three-dimensional profile of the X-ray beam at the sample position. Intensity is shown in arbitrary units. (*c*) Photon flux (photons s^{-1}) at the sample position as a function of energy and beam-defining aperture used.

Table 2
Sample environment and experiment control, ID29.

Diffractometer	MD2 microdiffractometer (MAATEL, Voreppe, France; Perrakis *et al.*, 1999); BGO, scintillator crystal for beam visualization at the sample position
Sample changer	Grenoble SC3 (Cipriani *et al.*, 2006); 50 sample capacity; SPINE standard sample holders; unloading/loading/ automatic loop centring ∼70 s
Fast shutter	Piezo-based millisecond shutter (CEDRAT, Meylan, France); opening/closing times ∼4 ms
Beam-defining apertures	Diameter 75 μm, 50 μm, 30 μm, 20 μm, 10 μm (MAATEL, Voreppe, France)
Fluorescence detector	XFlash 1000 (Bruker AXS, Madison, WI, USA)
Detector	PILATUS 6M pixel detector (DECTRIS, Baden, Switzerland); active area 435 (H) mm × 424 (V) mm; sample-to-detector distance 150–800 mm
Experiment control	*MxCuBE* GUI (Gabadinho *et al.*, 2010); allows for remote operation
Crystal characterization	*EDNA* (Incardona *et al.*, 2009), *BEST* (Bourenkov & Popov, 2010)
Beamline database	ISPyB (Beteva *et al.*, 2006; Delagenière *et al.*, 2011)

available upon request of external users for experiments at energies higher than 9.6 keV.

Focusing of the X-ray beam is achieved using an Rh-coated toroidal mirror equipped with a pneumatically driven bender (see Nurizzo *et al.*, 2006, for full details). A demagnification ratio of 3:1 [Fig. 1(*a*), Table 1] produces, at the sample position, a relatively small focal spot [30 μm × 60 μm; V × H, FWHM; Fig. 2(*b*)] containing ∼4.5 × 10^{12} photons s^{-1} at E = 11.56 keV (λ = 1.07 Å; Pt L_{III} absorption edge).

To aid trouble shooting and automated alignment, diagnostic elements have been strategically positioned in the OH. These diagnostic elements are essentially those described for ESRF beamline ID23-1 (Nurizzo *et al.*, 2006) which have been rolled out to all ESRF MX MAD beamlines.

3. Experimental set-up

All equipment in the EH, except for a set of three WAGO-controlled compressed-air-operated monochromatic beam attenuator boxes and a recently installed harmonic rejection mirror (see §3.2), is mounted on the 'experiment table', a block of granite mounted on three motorized vertical legs with two motorized horizontal translation stages. A major advantage of this design for a beamline equipped with a CCM is that, once beam-defining or beam-cleaning slits, goniometer rotation axis and sample position have been aligned to the X-ray beam, any realignment required as the result of beam movements (*i.e.* as the result of an energy change) is straightforwardly accomplished by a displacement of the granite block rather than a series of individual movements for each of the elements to be realigned.

3.1. Sample environment

The sample environment of ID29 [Fig. 1(*b*), Table 2] replicates the ESRF MX standard (McCarthy *et al.*, 2009; Leonard *et al.*, 2007) with the exception that an MD2 microdiffractometer (MAATEL, Voreppe, France; Perrakis *et al.*, 1999) is installed (Fig. 1*b*).

Photon flux at the sample position is relatively constant in the energy range most commonly used for MAD/SAD experiments but drops off either side of this (Fig. 2*c*). X-ray beam intensity is constantly monitored after the beam-cleaning slits in the EH using a scattering foil diode (I0), read through a Novelec amplifier and a WAGO device. The I0 reading is periodically correlated with photon flux using a previously calibrated diode placed at the sample position.

Daniele de Sanctis *et al.* · Beamline ID29 at ESRF   **457**

This calibration is repeated at different energies and for the different beam-defining apertures (see below). Sample exposure to X-rays is controlled using a piezo-based millisecond shutter (CEDRAT, Meylan, France).

The automatic mounting and unmounting of samples contained in SPINE standard sample holders is carried out with an SC3 robotic sample changer (Cipriani *et al.*, 2006). XANES (X-ray absorption near-edge structure) measurements around absorption edges and the collection of X-ray fluorescence spectra (Leonard *et al.*, 2009) are performed using an XFlash 1000 X-ray fluorescence detector (Bruker AXS, Madison, WI, USA). As already described (McCarthy *et al.*, 2009), for XANES measurements fluorescence is monitored during a continuous motion of the monochromator and a complete scan around an absorption edge is typically achieved in 20–30 s.

Experiment control is carried out using the *MxCuBE* GUI (Gabadinho *et al.*, 2010) which also allows for the remote control of the beamline (Gabadinho *et al.*, 2008). Photon flux at the sample position (see above) is both displayed in the *MxCuBE* GUI and automatically passed to *EDNA/BEST* crystal characterization (Incardona *et al.*, 2009; Bourenkov & Popov, 2010) when this is run from the GUI. Experiment tracking and logging is carried out using the ISPyB database (Beteva *et al.*, 2006; Delagenière *et al.*, 2011).
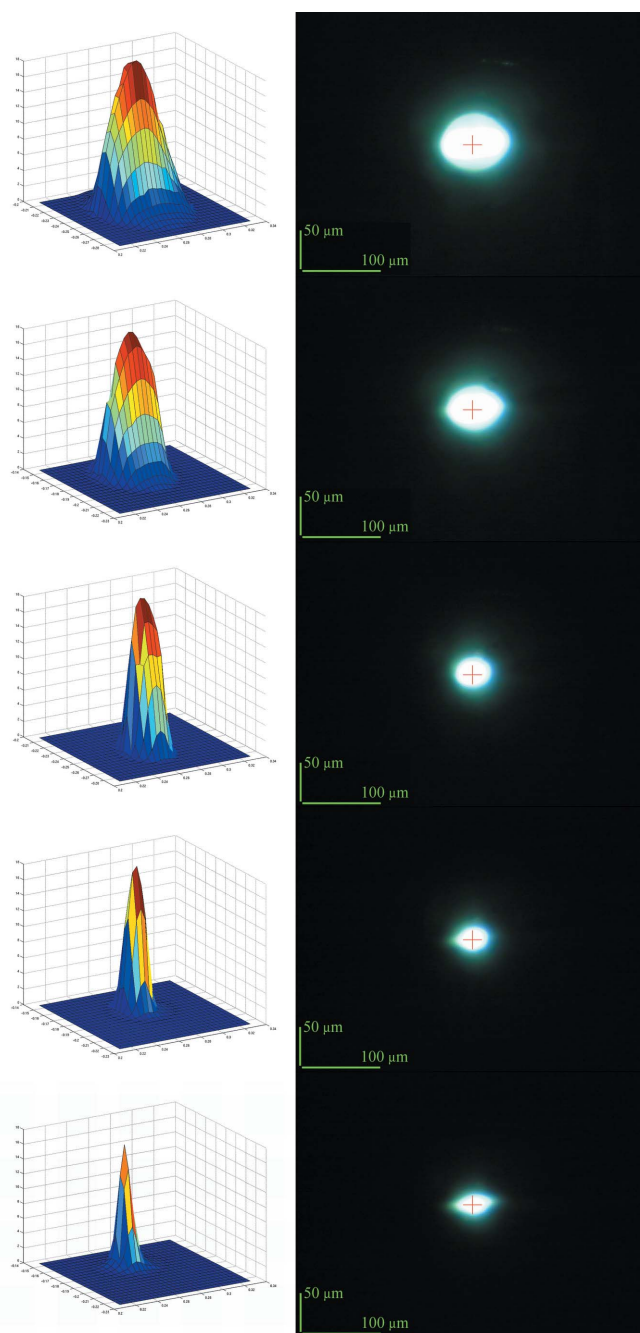
The MD2 installed on ID29 has also been equipped with a series of apertures, 75 µm, 50 µm, 30 µm, 20 µm and 10 µm in diameter, mounted on a vertical/horizontal translation stage (Fig. 1*b*). The device is similar in nature to that described for the GM/CA-CAT insertion-device beamlines 23ID-D and 23ID-B at the Advanced Photon Source (Sanishvili *et al.*, 2008) and can, *via MxCuBE*, be used to rapidly change the size of the X-ray beam impinging on the sample (Fig. 3). The flux density at the sample position with the 10 µm aperture inserted ranges from $\sim 6.4 \times 10^8$ photons s^{-1} µm^{-2} at ~ 12 keV ($\lambda \simeq 0.97$ Å) to $\sim 4 \times 10^7$ photons s^{-1} µm^{-2} at the extremes of the energy range routinely available on the beamline. Thus, despite not being a microfocus beamline, ID29 is, particularly in the middle of the available energy range, a suitable facility on which to perform MAD/SAD experiments on micro-crystals.[1] Other reasons why one might wish to change the beam size at the sample position include: matching beam and sample sizes, the use of a smaller beam in helical data collection protocols (Flot *et al.*, 2010); grid and mesh scans (Bowler *et al.*, 2010; Aishima *et al.*, 2010); accurate diffraction-based crystal centring (Song *et al.*, 2007).

3.2. Harmonic rejection

As already described (McCarthy *et al.*, 2009), ESRF CCMs have a 'weak link' between the two diffracting surfaces. The pitch of the second face can be adjusted using a motorized thin metal blade (a 'pusher') which deforms the weak link, allowing both the scanning of the rocking curves and the rejection, when working at softer energies, of higher harmonic contaminants of the X-ray beam not rejected by the focusing mirror. However, while offsetting the rocking curves of the two diffracting faces of the CCM efficiently eliminates higher harmonic contamination, it also reduces the intensity of the primary component of the X-ray beam. This reduction in intensity is of the order of 50% depending on the wavelength.
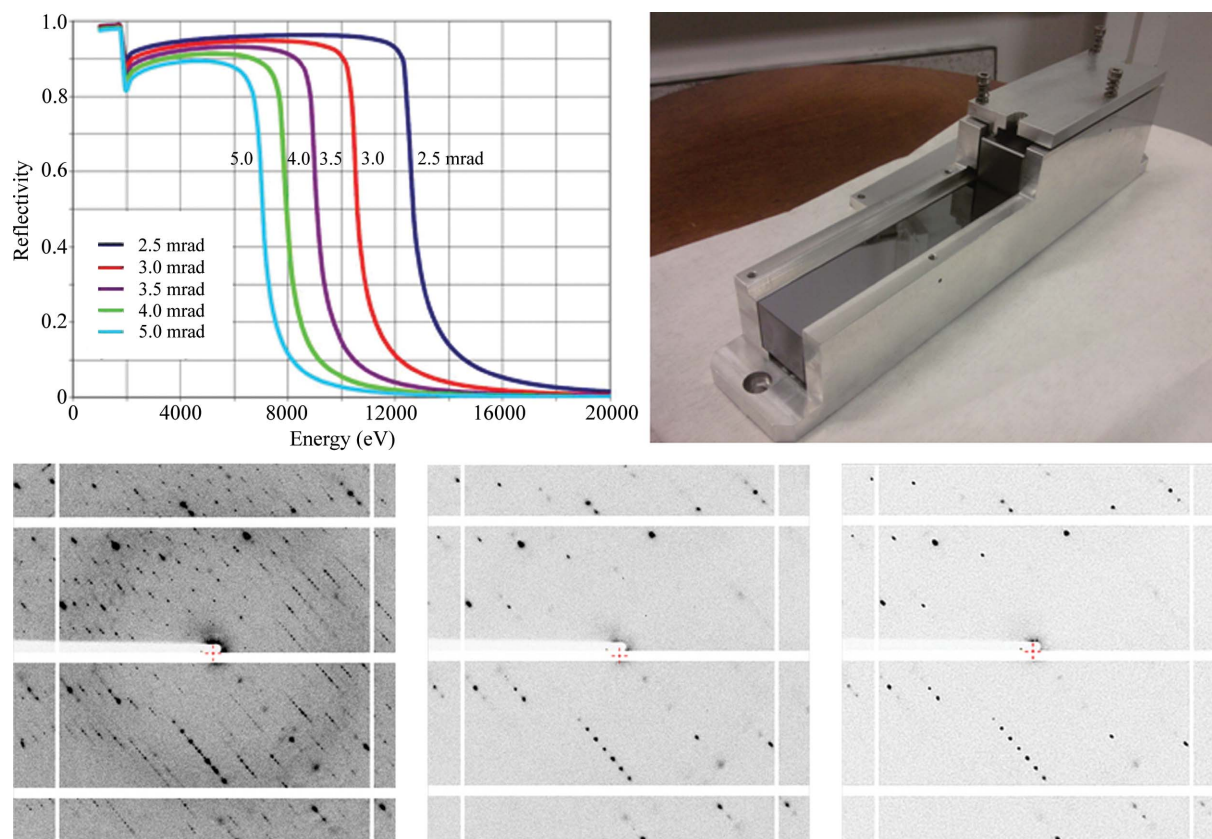
An excellent alternative to this monochromator detuning is the introduction, close to the sample, of a flat silicon mirror. At low grazing angles, and at the softer end of the energy range at which ID29 operates, such mirrors have high reflectivity in the energy range

Figure 3
X-ray beam sizes available on ID29. Three-dimensional profiles (left) and the appearance on the BGO scintillator crystal (right) of the X-ray beam at the sample position with (from top to bottom) 75 µm, 50 µm, 30 µm, 20 µm and 10 µm beam-defining apertures inserted. Intensity is shown in arbitrary units.

of the principle energy component of the X-ray beam and no reflectivity of higher harmonic contaminants (Fig. 4). This allows the efficient rejection of higher harmonic reflections without a significant reduction in the intensity of the low-energy X-rays impinging on the sample. Such a mirror (grazing angle 3 mrad) was installed and commissioned on ID29 and inserted into the beam path when a photon energy of $E < 9.0$ keV is chosen. However, while the rejection of higher harmonic contaminants was satisfactory and flux at the sample position increased, routine use of the system was difficult. The system was thus modified by the addition of a second mirror (Fig. 4). This double-mirror system results in the path of the deflected beam

---

[1] For comparison, the flux density available on the fixed-wavelength ($E \simeq 14.2$ keV; $\lambda \simeq 0.837$ Å) ESRF micro-focus beamline ID23-2 (focal spot 5 µm × 7 µm; V × H, FWHM) is $\sim 2 \times 10^9$ photons s^{-1} µm^{-2} (Flot *et al.*, 2010).

Figure 4
The rejection of higher harmonic contaminants on ID29. Top left: a plot of reflectivity *versus* photon energy for the flat Si mirrors used in the ID29 higher harmonic rejection system. Top right: the double-mirror system installed. Bottom: diffraction images collected at $\lambda = 2.07$ Å ($E = 6.0$ keV) showing the third-harmonic rejection obtained using the Si double-mirror system (right) and the Si(111) CCM pusher system (middle). For comparison, a diffraction image collected when no harmonic rejection was carried out is also shown (left). The diffraction pattern of the latter is clearly badly contaminated.

being parallel to that of the undeflected beam and limits realignment of the experimental table to a simple vertical movement of ~0.8 mm (*i.e.* twice the vertical separation of the mirrors). Use of the upgraded system, which is currently under commissioning, will thus be much more straightforward, easier to automate and its use will no longer be limited to expert users of the beamline. The insertion of a second mirror will increase the efficiency of the rejection of harmonic contaminants with an energy of 18 keV from about 10^{-2} to ~10^{-4}.

3.3. Detector

ID29 is equipped with a PILATUS 6M pixel detector (DECTRIS, Baden, Switzerland). The PILATUS 6M provides an increased detection area, and improved dynamic range, point-spread function and detective quantum efficiency (particularly at longer wavelengths) when compared with currently available CCD-based devices. The extremely fast readout (~2 ms) of the detector coupled with a possible 12 Hz frame rate also allows for the collection of diffraction data in a continuous rotation, a so-called shutterless mode (Hülsen *et al.*, 2006; Broennimann *et al.*, 2006), coupled with fine φ-sliced oscillation images.

Helical data collection (Flot *et al.*, 2010) is enabled with two different options. In the first case, a stepped helical scan; the number of discrete positions along the crystal from which data are to be collected is automatically calculated as a function of start and end points on the crystal (user defined) and the X-ray beam size. The number of images to be collected at each position is calculated

from the oscillation range for individual images and the total oscillation range required. While at each discrete position data are collected in shutterless mode, the shutter is closed while translating from one discrete position to the next. The second option implemented on ID29 allows for a continuous helical scan. Here, the centring and alignment motors of the MD2 are synchronized with the goniostat rotation axis in such a way that, during the entire rotation range desired, the sample is continuously translated, at constant speed, along the direction defined by the crystal start and end points for data collection. In this case, diffraction images are not collected from discrete positions along the crystal and the shutter remains open during the entire data collection. A comparison of the data quality resulting from use of these two protocols is shown in Table 3.

To cope with the sustained high levels of data produced (72 MB s^{-1} when operating in shutterless mode at 12 Hz), the detector has its own bespoke computing environment (Fig. 5). Raw images are written in the RAMDISK of the detector control PC (pilatus29 in Fig. 5), immediately transformed to mini-CBF (crystallographic binary format; Bernstein & Hammersley, 2006) and transferred *via* a dedicated 10 Gb s^{-1} link to a holding computer (id29gate in Fig. 5) equipped with 4 × 600 GB fast (15000 rpm) SAS (Serial Attached SCSI) disks mounted in hardware RAID 0 with a writing performance better than 300 MB s^{-1}. During data collection, diffraction images are automatically displayed on the beamline control computer using *ADXV* (Szebenyi *et al.*, 1997; Area Detector Systems Corporation, San Diego, USA; http://www.scripps.edu/~arvai/
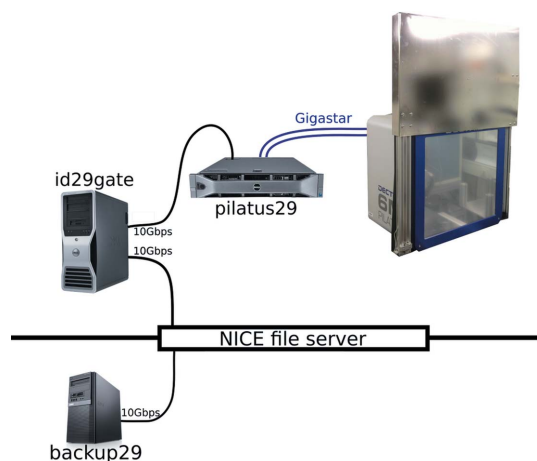
Table 3
Data quality statistics from *XDS* (Kabsch, 2010) for diffraction data collected from a crystal of bovine trypsin crystal (space group $P2_12_12_1$; $a = 60.2$ Å, $b = 64.1$ Å, $c = 69.9$ Å) employing either the stepped helical (*A*) or continuous helical (*B*) scans described in the main text.

d_{min} (Å)	Observed	Unique	Comp (%)	R_{sym} (%)	R_{meas} (%)	$\langle I/\sigma(I)\rangle$
A						
4.48	7161	1775	98.0	3.8	4.3	32.86
3.17	12521	3028	98.2	3.7	4.2	32.82
2.59	15997	3883	98.7	3.9	4.5	30.00
2.25	18908	4540	98.7	4.4	5.0	27.12
2.01	22357	5151	99.3	5.0	5.8	23.45
1.84	23792	5670	99.2	6.1	7.1	17.51
1.70	25294	6163	99.3	7.9	9.1	12.16
1.59	15041	5960	90.1	8.7	10.8	6.94
1.50	8642	4601	65.1	10.7	13.9	4.29
Total	149713	40771	92.2	4.1	4.7	18.48
B						
4.48	7109	1761	97.5	3.8	4.3	34.53
3.17	12455	3013	98.2	3.6	4.1	34.53
2.59	15943	3879	98.8	3.6	4.2	31.95
2.25	18786	4510	98.5	4.0	4.6	29.39
2.01	22230	5136	99.4	4.4	5.1	25.96
1.84	23716	5643	98.9	5.4	6.2	20.04
1.70	25215	6113	99.2	6.8	7.8	14.53
1.59	15174	5967	90.3	7.4	9.2	8.55
1.50	8709	4642	66.0	8.6	11.2	5.38
Total	149337	40664	92.3	3.9	4.5	20.47

Table 4
Statistics from *XDS* (Kabsch, 2010) processing of data collected using the Pilatus 6M detector in shutterless mode from a crystal of bovine trypsin (space group $P3_121$; $a = b = 54.5$ Å, $c = 107.1$ Å).

A: fine φ-slicing ($\Delta\varphi = 0.1°$), individual images processed. *B*: images from dataset *A* merged using *MERGE2CBF* (Kabsch, 2010) to produce images with $\Delta\varphi = 1.0°$ which were then processed with *XDS*.

d_{min} (Å)	Observed	Unique	Comp (%)	R_{sym} (%)	R_{meas} (%)	$\langle I/\sigma(I)\rangle$
A						
4.24	8264	1473	99.5	2.4	2.6	60.86
3.00	15173	2501	99.8	2.6	2.7	60.80
2.45	19988	3193	99.9	3.0	3.0	50.98
2.13	24291	3746	99.9	3.5	3.5	42.93
1.90	26674	4187	99.8	4.3	4.5	32.47
1.74	25745	4493	97.5	5.8	6.8	20.39
1.61	14132	4091	82.0	7.8	10.3	10.03
1.50	7553	3389	62.9	11.2	14.9	5.31
1.42	2178	1442	25.4	16.7	21.1	3.02
Total	143998	28515	79.6	3.0	3.1	30.03
B						
4.23	8290	1474	99.5	2.3	2.6	61.87
3.00	15214	2503	99.8	2.5	2.6	60.79
2.45	20081	3191	99.8	3.2	3.1	49.14
2.12	24349	3744	99.9	3.8	3.8	39.90
1.90	26683	4189	99.8	5.0	5.2	29.01
1.73	25645	4492	97.4	7.0	8.2	17.50
1.61	14081	4081	81.7	9.9	12.9	8.40
1.50	7591	3395	63.0	14.9	18.9	4.42
1.42	2186	1455	25.6	24.3	26.6	2.50
Total	144120	28524	79.7	3.1	3.3	28.14

`adxv.html`). The refresh rate is around 1 s, with about one in every ten images being displayed.

At the end of each data collection, images are copied over a 10 Gb s^{-1} connection from id29gate to the ESRF central storage system from which images are available for further analysis and backup. As soon as the first image of a data collection appears on the central storage disks, a preliminary round of autoprocessing (Monace *et al.*, in preparation) of the images (integration, scaling) is started. Once all images have been transferred, a more complete round of processing is performed. Results are displayed in the ISPyB Laboratory Management Information System (Beteva *et al.*, 2006; Delagenière *et al.*, 2011).

As has already been reported (Hülsen *et al.*, 2006), when using a pixel-based detector, data sets collected using fine φ-slicing display better quality at high resolution than those collected using a more conventional oscillation range. However, collecting fine φ-sliced data sets results in many more individual oscillation images to be backed up or processed. For those users who wish to reduce the number of

Figure 5
The computing infrastructure used in the integration of a Pilatus 6M pixel detector on ID29.

images produced, the *MxCuBE* GUI on ID29 now provides the possibility to automatically merge images from fine φ-sliced data sets. This procedure uses the program *MERGE2CBF* (Kabsch, 2010). The merged diffraction images have corrected headers, can be processed with standard software such as *XDS* (Kabsch, 2010) or *MOSFLM* (Leslie, 2006) and result in intensity data with only a slightly degraded quality compared with those obtained when images from the initial fine φ-sliced data sets are processed individually (Table 4).

3.4. Ancillary techniques on ID29

The ESRF places emphasis on the use of techniques complementary to X-ray crystallography. One such technique, *in crystallo* spectroscopy, is available on ID29 *via* the ESRF Cryobench Laboratory, ID29S http://www.esrf.fr/UsersAndScience/Experiments/MX/Cryobench. Novel experimental set-ups, which will be described elsewhere, have been designed for carrying out on-line (*i.e.* at beamline) Raman and fluorescence spectroscopic analyses. These set-ups are available to users of ID29 upon prior request. The same set-up can be easily adapted for UV-RIP phasing experiments (Nanao *et al.*, 2005; Panjikar *et al.*, 2011; de Sanctis *et al.*, 2011).

4. Perspectives

4.1. Short and medium term

As outlined in §3.1, the ability, using apertures, to reduce the size of the X-ray beam impinging on the sample to $\sim$10 µm in diameter makes ID29 a suitable facility on which to perform experiments on all but the smallest of microcrystals. However, with a 10 µm aperture in place, the flux density available is rather low at softer energies ($\sim$3.2 $\times$ 10^7 photons s^{-1} µm^{-2} at 6 keV). Thus, at these energies, experiments on microcrystals would be rather time-consuming. The short- and medium-term perspectives for ID29 thus involve improving the photon flux available at softer energies and extending its routinely usable range to even longer wavelengths. This will have significant

advantages. The derivatization of protein crystals with elements such as Xe (Schiltz *et al.*, 1994, 2003; Sauer *et al.*, 1997) or I (Beck *et al.*, 2008, 2010; Evans & Bricogne, 2002) is becoming more common. The Xe L_I absorption edge is at 5.45 keV (λ = 2.27 Å), that of I at 5.18 keV (λ = 2.39 Å). Optimized SAD experiments targeting these absorption edges would yield $f'' \simeq 13$ e$^-$ while for MAD experiments a $\Delta f'$ of ~9 e$^-$ can easily be induced. Such a combination of large anomalous and dispersive signals from these two elements is only possible with the use of softer X-rays.

Currently the diamond window in the ID29 front-end absorbs about 60% of the photons at 6 keV. Major gains in sample position flux at softer energies would thus be made by removing this and placing the front end in an ultra-high-vacuum (UHV) configuration. Additional gains in the flux available at softer energies would be made by placing the path between the exit window of the beamline and the sample under helium or rough vacuum rather than, as is currently the case, air. Coupling these actions with a microfocus, rather than the current microbeam, approach would significantly increase flux densities at softer energies and create at the ESRF a wide-energy-range, fully tunable, microfocus facility for macromolecular crystallography experiments exploiting anomalous scattering.

4.2. Long term

The longer-term future of ID29 must be seen in the context of the current upgrade of the ESRF storage ring and experimental facilities (http://www.esrf.eu/AboutUs/Upgrade). The increase in the useful length of straight sections, planned in the ESRF Upgrade Programme, to 6 m will allow the undulator configuration of ID29 to be optimized. Options here include the addition of a second 1.6 m ESRF U$_{35}$ undulator device in order to further improve photon fluxes at lower energies [Fig. 2(*a*); 3.2 m U$_{35}$ plus 2.0 m U$_{21}$]. This, coupled with an UHV environment (see above), would significantly extend the potential operating range of ID29 and photon flux at energies as low as 3.5 keV would be considerable. This would make MAD/SAD experiments around the M_V and M_{IV} absorption edges of U possible. Such experiments may, in the future, prove useful for the phasing of very large macromolecular complexes (see Liu *et al.*, 2001, for a discussion of this).

The extension of the experimental hall, also planned in the ESRF Upgrade Programme, means that, if there is a clear scientific need, ID29 could be re-constructed as a 'long' (~120 m) beamline. Here, the much larger demagnification ratios available would result in very small focal spot sizes at the sample position. Indeed, the recent achievement of the ESRF Accelerator Division in reducing the electron beam vertical emittance on the ESRF machine by a factor of six (http://www.esrf.fr/news/spotlight/spotlight115/spotlight115/) suggests that a 'long' ID29 could, employing refractive lenses and/or zone plate focusing devices, produce a focal spot of submicrometre size at the sample position. Which, if any, of the longer-term options described above will be implemented will be decided only after extensive discussions with the ESRF's external user community.

References

Aishima, J., Owen, R. L., Axford, D., Shepherd, E., Winter, G., Levik, K., Gibbons, P., Ashton, A. & Evans, G. (2010). *Acta Cryst.* D**66**, 1032–1035.

Beck, T., Gruene, T. & Sheldrick, G. M. (2010). *Acta Cryst.* D**66**, 374–380.

Beck, T., Krasauskas, A., Gruene, T. & Sheldrick, G. M. (2008). *Acta Cryst.* D**64**, 1179–1182.

Berman, H. M., Westbrook, J., Feng, Z., Gilliland, G., Bhat, T. N., Weissig, H., Shindyalov, I. N. & Bourne, P. E. (2000). *Nucleic Acids Res.* **28**, 235–242.

Bernstein, H. J. & Hammersley, A. P. (2006). *International Tables for Crystallography*, Vol. G, pp. 37–43. Heidelberg: Springer.

Beteva, A. *et al.* (2006). *Acta Cryst.* D**62**, 1162–1169.

Biasci, J.-C., Plan, B. & Zhang, L. (2002). *J. Synchrotron Rad.* **9**, 44–46.

Biou, V., Leonard, G., Stojanoff, V., Labouré, S., Mattenet, M., Helliwell, J., Felizaz, F., Claustre, L., Lapeyre, F., Brown, K. & Thompson, A. (1997). *ESRF Newsl.* **28**, 21–25.

Bourenkov, G. P. & Popov, A. N. (2010). *Acta Cryst.* D**66**, 409–419.

Bowler, M. W., Guijarro, M., Petitdemange, S., Baker, I., Svensson, O., Burghammer, M., Mueller-Dieckmann, C., Gordon, E. J., Flot, D., McSweeney, S. M. & Leonard, G. A. (2010). *Acta Cryst.* D**66**, 855–864.

Broennimann, Ch., Eikenberry, E. F., Henrich, B., Horisberger, R., Huelsen, G., Pohl, E., Schmitt, B., Schulze-Briese, C., Suzuki, M., Tomizaki, T., Toyokawa, H. & Wagner, A. (2006). *J. Synchrotron Rad.* **13**, 120–130.

Cipriani, F. *et al.* (2006). *Acta Cryst.* D**62**, 1251–1259.

Delagenière, S. *et al.* (2011). *Bioinformatics*, **27**, 3186–3192.

Evans, G. & Bricogne, G. (2002). *Acta Cryst.* D**58**, 976–991.

Flot, D., Mairs, T., Giraud, T., Guijarro, M., Lesourd, M., Rey, V., van Brussel, D., Morawe, C., Borel, C., Hignette, O., Chavanne, J., Nurizzo, D., McSweeney, S. & Mitchell, E. (2010). *J. Synchrotron Rad.* **17**, 107–118.

Gabadinho, J., *et al.* (2010). *J. Synchrotron Rad.* **17**, 700–707.

Gabadinho, J., Hall, D., Leonard, G., Gordon, E., Monaco, S. & Thibault, X. (2008). *Synchrotron Radiat. News*, **21**, 21–29.

Hülsen, G., Broennimann, C., Eikenberry, E. F. & Wagner, A. (2006). *J. Appl. Cryst.* **39**, 550–557.

Incardona, M.-F., Bourenkov, G. P., Levik, K., Pieritz, R. A., Popov, A. N. & Svensson, O. (2009). *J. Synchrotron Rad.* **16**, 872–879.

Kabsch, W. (2010). *Acta Cryst.* D**66**, 125–132.

Leonard, G., McCarthy, J., Nurizzo, D. & Thibault, X. (2007). *Synchrotron Radiat. News*, **20**, 18–24.

Leonard, G., Solé, V. A., Beteva, A., Gabadinho, J., Guijarro, M., McCarthy, J., Marrocchelli, D., Nurizzo, D., McSweeney, S. & Mueller-Dieckmann, C. (2009). *J. Appl. Cryst.* **42**, 333–335.

Leslie, A. G. W. (2006). *Acta Cryst.* D**62**, 48–57.

Liu, Y., Ogata, C. M. & Hendrickson, W. A. (2001). *Proc. Natl Acad. Sci. USA*, **98**, 10648–10653.

McCarthy, A. A., Brockhauser, S., Nurizzo, D., Theveneau, P., Mairs, T., Spruce, D., Guijarro, M., Lesourd, M., Ravelli, R. B. G. & McSweeney, S. (2009). *J. Synchrotron Rad.* **16**, 803–812.

Nanao, M. H., Sheldrick, G. M. & Ravelli, R. B. G. (2005). *Acta Cryst.* D**61**, 1227–1237.

Nurizzo, D., Mairs, T., Guijarro, M., Rey, V., Meyer, J., Fajardo, P., Chavanne, J., Biasci, J.-C., McSweeney, S. & Mitchell, E. (2006). *J. Synchrotron Rad.* **13**, 227–238.

Panjikar, S., Mayerhofer, H., Tucker, P. A., Mueller-Dieckmann, J. & de Sanctis, D. (2011). *Acta Cryst.* D**67**, 32–44.

Perrakis, A., Cipriani, F., Castagna, J.-C., Claustre, L., Burghammer, M., Riekel, C. & Cusack, S. (1999). *Acta Cryst.* D**55**, 1765–1770.

Sanctis, D. de, Tucker, P. A. & Panjikar, S. (2011). *J. Synchrotron Rad.* **18**, 374–380.

Sanishvili, R., Nagarajan, V., Yoder, D., Becker, M., Xu, S., Corcoran, S., Akey, D. L., Smith, J. L. & Fischetti, R. F. (2008). *Acta Cryst.* D**64**, 425–435.

Sauer, O., Schmidt, A. & Kratky, C. (1997). *J. Appl. Cryst.* **30**, 476–486.

Schiltz, M., Fourme, R. & Prange, T. (2003). *Method Enzymol.* **374**, 83–119.

Schiltz, M., Prangé, T. & Fourme, R. (1994). *J. Appl. Cryst.* **27**, 950–960.

Song, J., Mathew, D., Jacob, S. A., Corbett, L., Moorhead, P. & Soltis, S. M. (2007). *J. Synchrotron Rad.* **14**, 191–195.

Szebenyi, D. M. E., Arvai, A., Ealick, S., LaIuppa, J. M. & Nielsen, C. (1997). *J. Synchrotron Rad.* **4**, 128–135.

Wakatsuki, S., Belrhali, H., Mitchell, E. P., Burmeister, W. P., McSweeney, S. M., Kahn, R., Bourgeois, D., Yao, M., Tomizaki, T. & Theveneau, P. (1998). *J. Synchrotron Rad.* **5**, 215–221.